Hindawi
Journal of Nanotechnology
Volume 2023, Article ID 8638512, 8 pages
https://doi.org/10.1155/2023/8638512

Research Article

The Role of Annealing Treatment on Crystallographic, Optical, and Electrical Features of Bi_2O_3 Thin Films Prepared Using Reactive Plasma Sputtering Technology

Sabeeha A. J. Beden,[1] **Hassan A. Dumboos**,[2] **Mustafa K. Ismael**,[3] **and Mohanad Kadhim Mejbel**[1]

[1]*Middle Technical University, Technical Engineering College-Baghdad, Baghdad 10001, Iraq*
[2]*Ministry of Science and Technology, MOST Baghdad 10001, Iraq*
[3]*Middle Technical University, Institute of Technology, Baghdad 10001, Iraq*

Correspondence should be addressed to Mohanad Kadhim Mejbel; mohanad@mtu.edu.iq

Received 15 March 2023; Revised 9 May 2023; Accepted 1 June 2023; Published 9 June 2023

Academic Editor: Sivakumar Manickam

Bismuth oxide (Bi_2O_3) has attracted considerable research interest in test thin films made utilizing the reactive plasma sputtering (RPS) technology-assisted annealing treatment, allowing the development of diverse Bi_xO_x thin films. SEM, phase X-ray diffraction patterns, UV-Vis spectrometers, and D.C. two-probes are used to identify the crystallographic structure and assess the films' optical-electrical properties. The XRD examination showed that forming Bi_2O_3 films with an amorphous to multiphase crystalline structure for sputtering time of 40 min was due to soda glass substrate temperature at a range of 30–35°C. Thin films of Bi_2O_3 crystal structures improved with annealing heat treatment at 200, 300, 400, and 500°C. Yet the formation of crystalline phase (β-Bi_2O_3 with δ-Bi_2O_3) Bi_2O_3 nanostructures occurred at higher temperatures. SEM images showed transparent particles highly affected by annealing temperatures. The nanostructures were about 102–510 nm long, and the diameter was 50–100 nm. The Bi_2O_3 film optical band gaps and nanostructures ranged from 2.75 to 3.05 eV. The annealing temperature differences affected the crystallite sizes, optical band gaps, and surface roughness. The findings showed that these differences caused the phase transition in Bi_2O_3 structures. The electrical calculation revealed that the electrical conductivity improved with annealing temperatures of 150–250°C while declining with temperature (300–500)°C with typical semiconductor films.

1. Introduction

There is a considerable number of Bi_2O_3 films which are very striking. The same is true with nanostructures because they are optical and electrical, including their wide energy band gap, the dielectric permittivity refractive index, Bi_2O_3, impressive photoluminescence, photoconductivity optoelectronics, gas sensors, Schottky barrier optical coatings, and metal-insulator-semiconductor capacitors. Furthermore, solar cells and microwaves are also integrated into the circuits [1–11]. Generally, physical [12, 13], and chemical [14–16], and electrodeposition methods [17] were developed for preparing different bismuth nanostructures like nanoparticles [16], triangular nanoplate [18], nanotubes [19, 20], nanowires [21], and nanospheres [22]. Bi_2O_3 contains the following vital polymorphic phases: α-, β-, γ-, δ, and ε-Bi_2O_3. According to the crystal structures, the Bi_2O_3 optical band gap ranges from 3.6 eV to 1.7 eV [3, 23]. The phases show various forms and different physical or electrical features. Thus, the use of Bi_2O_3's other main applications is practical. The annealing temperature differences affect the crystallite sizes, optical band gaps, and surface porosities [3, 23]. The phases show various forms and different physical or electrical features. Thus, the use of Bi_2O_3's other main applications is practical. The annealing temperature differences affect the crystallite sizes, optical band

gaps, and surface porosities. Some studies [24, 25] showed that these differences (often in oxidation) caused the transition in Bi_2O_3 structures. Yet, investigating reactive plasma-assisted annealing's ability to form Bi_2O_3 films or nanostructures has been a lonesome field [26, 27]. Some works discuss extensively, such as film-based transistors using indium zinc tin oxide (IZTO) semiconducting thin film by Bak et al. [28] and low-temperature growth of crystalline tin (II) monosulfide thin films using atomic layer deposition (ALD) by Ansari et al. [29] Authors studied the influence of postannealing on the structural optical and electrical properties of SnN_x thin films [30]. Moreover, researchers are investigating bismite nanoisland thin films for optoelectronics, which have a narrow bandgap of 1.95 eV with suitable properties for nonlinear optoelectronics [31]. However, various film deposits obtain specific properties. For gas sensors, Rasheed et al. [32] developed (NiO : Zn) thin films by easy chemical spray pyrolysis, and for optical properties, Najim [33] and Hassan [34] created nanocrystalline Ba-doped Mn_3O_4 and Co-doped ZnO thin films, showing that the band gap decreases with increasing Co doping concentrations for ZnO thin films and is improved by increasing Ba doping for Mn_3O_4.

The current work examined the temperature of the substrate influence on growing, phase compositing, and electrical and optical features of Bi_2O_3 structures made through reactive plasma-assisted annealing treatment. The approach is straightforward and economical with no additives, including surfactants, template agents, and more metal oxides with ions following the transition.

2. Experimental Setup

The plasma sputtering devices are fully illustrated in Figure 1(a), which consists of a chamber of ionization linked to a chamber of sputtering by one aperture with a pressure decrease (see Figure 1(b)). A heated tantalum filament discharges the electrons into the ionization chambers and the argon gas emission onsets by the auxiliary anodes. An arc discharge is latched between the hot cathodes and anodes in the sputtering chamber. To hasten the arc plasma quickly to the Bi bulk aim to sputter the material, a negative voltage is applied on the target, driving the ions.

There is a deposition of Bi_2O_3 thin films onto soda lime glass substrates through the reactive plasma helped by the annealing step with a 10°C min^{-1} heating over 2 hours in the air furnace and then cooled to ambient temperatures (see Figure 1(c)). The glass substrates are fixed 50 mm from the target and with temperature substrate during sputtering at a range of 30–35°C and 1.5×10^{-2} mbar pressure with a 5% O_2 flow rate. The sputtering process would involve bombarding the Bi target with high-energy ions to sputter Bi atoms from the target to deposit Bi_2O_3 thin films. The sputtered Bi atoms would then interact with an oxygen source, such as a reactive oxygen gas, in the vacuum chamber to form Bi_2O_3 molecules. These Bi_2O_3 molecules would then deposit onto the substrate to start a thin film. It is important to note that the deposition conditions, such as the power input, gas pressure, and substrate temperature, would need to be optimized to obtain the desired Bi_2O_3 film properties, such as the composition, thickness, and microstructure. Additionally, the resulting Bi_2O_3 thin films are characterized using various analytical techniques to confirm their properties. The samples applied to annealing treatment temperatures (200, 300, 400, and 500°C) were signed as S1, S2, S3, and S4. Metallic Bi bulk disc (Kurt J. Lesker Company-UK, 99.999% purity) of 50 gm was used as the target material. We cleaned the glass substrates ultrasonically for 20 minutes with acetone and deionized water before drying them in the nitrogen flow. The creation of Ar-O plasma resisted the bismuth boat shield, and the substrate holders heated from room temperature to 35°C and negative during sputtering with the 2 kV bias voltage. The annealing process formed whitish yellow-coloured glass slides, as shown in Figure 1(c). A quartz crystal thin film monitor controls film thickness during deposition, while a Tencor Alpha Step profiler measures Bi_2O_3 film thickness following up the annealing process. SEM was utilized to examine the material's surface morphology (RAITH-e-LiNE, Raith GmbH) [35–40]. The voltage for the SEM images was 10 kV, and the distances used were 5.6 mm and 10.6 mm, respectively. By applying (Bragg–Brentano) geometry and monochromatic Cu-Kα radiation in X-ray diffraction (XRD) (Bruker D8 Advance) [36, 37, 41–47], we examined the thin film crystallographic structure. We calculated the film absorption spectra with UV-Vis spectrophotometers (ocean Optics USB 4000) [48–51] and determined the optical band gap Eg.

3. Results and Discussion

Sputtering of Bi particles in the oxygen atmosphere formed the Bi_2O_3, as $Bi + O_2 \longrightarrow Bi_2O_3$ [52, 53]. The sputtering rate of Bi_2O_3 rises when the oxygen pressure increases to $1.5 \times 10{-}2$ mbar for 40 min. The temperature of substrate annealing has a significant influence on the Bi_2O_3 film surface morphology. The surface structures in the SEM pictures are of Bi_2O_3 at various temperatures, as shown in Figure 2. The film was grown at an annealing temperature of 200°C and showed identical and quite dense structures with various grain sizes of 100–200 nm (Figure 2(a)). When the annealing temperature reached 300°C (see Figure 2(b)), the grain size shrank to 11–20 nm, and the gaps in the grain boundaries disappeared with a rise in the density. At temperatures of 200°C and 500°C, the thickness of Bi_2O_3 films was 606 nm and 571 nm, respectively. When the deposition was completed at higher temperatures of 400°C (see Figure 2(c)) and 500°C (see Figure 2(d)), nanostructures were formed on the surface. At 400°C, 3D nanostructures covered the surface with an irregular, branching morphology. Bi_2O_3 nanostructures have a length range of 100 to 500 nm and in diameter of 50–100 nm, as shown in Figure 2(d).The results show that changing the annealing temperature during the formation of the Bi_2O_3 structure changed the surface morphology of dense layers from one of low temperature to that of high temperature, leading to a lower nanostructure and its crystal.

The data for the XRD were obtained over the range of 20° to 70° with a 0.02° step and 0.2 s for data acquisition. The

FIGURE 1: (a) The reactive plasma sputtering system diagram, (b) the image of in-site lab system, and (c) glass lab slide samples with Bi_2O_3 thin films.

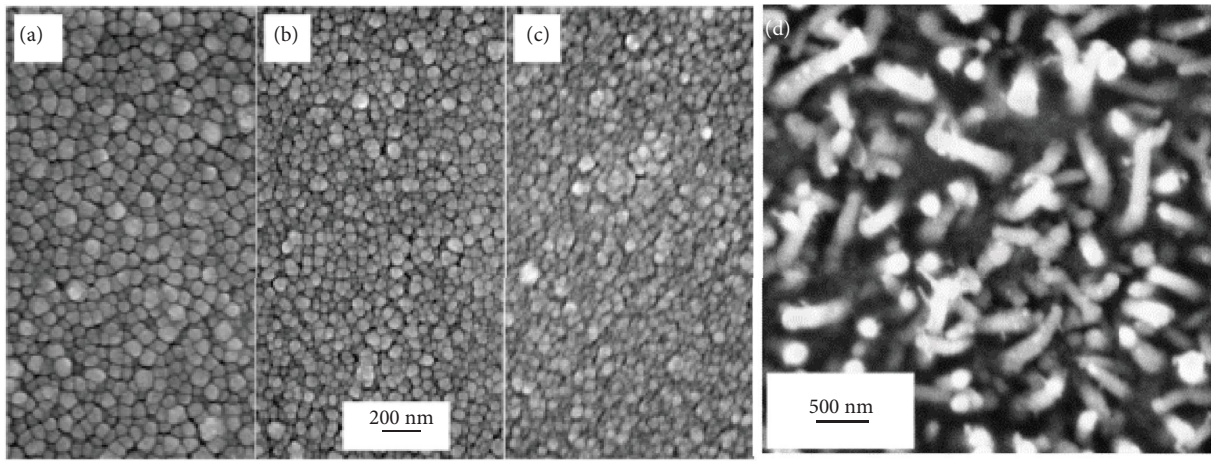

FIGURE 2: SEM Bi_2O_3 films and nanostructures being deposited at various substrate temperatures: (a) 200°C, (b) 300°C, (c) 400°C, and (d) 500°C.

phase identification process used the JCPDS PDF database 42. Figure 3 shows the amorphous Bi sample (S1 and S2) preannealing treatment, but S3 and S4 show some peaks in the transformation to crystallite phases. Annealing Bi_2O_3 films at 200°C showed the XRD pattern of low-intensity broad peak as shown in Figure 4. Elevating the temperature to 400°C creates the β-Bi_2O_3 phase with δ-Bi_2O_3 phase impurity. At 27.95°, a strong diffraction line with a tetragonal structure was ascribed to the (201) plane of β-Bi_2O_3. Additionally, at $2\theta = 31.66°$, the low-intensity peaks, with the (002), (220), (222), (203), (421), and (402) planes are responsible for the angles of 32.69°, 46.22°, 54.25°, 55.51°, and 57.80°, respectively. When Bi_2O_3 nanostructure formation happened at 400°C, the (201) direction was favoured.

The XRD demonstrated the formation of the single nanocrystalline phase of δ-Bi_2O_3. The appearance of the single nanocrystalline phase of δ-Bi_2O_3 was shown by the XRD nanowire patterns deposited at 500°C on a glass substrate (Figure 2(d)). The use of the face-centred cubic (fcc) structure at peaks $2\theta = 27.86°$ and 32.24° is possible for the identification of this phase, 49.29°, 54.92°, and 57.60°, which correspond to the (111), (200), (220), (311), and (222) orientation of one δ-Bi_2O_3 phase with a 5.4754 nm lattice parameter (JCPDS data file no. 47–1056). The XRD data determine crystallite sizes by conventional Scherer's formula for the average crystallite sizes of nanostructures made at 400°C and 500°C temperatures, respectively, 50.5 nm and 37.7 nm. Yet, the Bi_2O_3 stayed in an amorphous phase at a temperature less than 200°C; the peak narrowing of $2\theta = 27°$-28° showed atom rearrangement in bulk, and the energy stayed decreased for the film crystallizations, which conforms with previous research [54, 55]. The evaporation of the electronically excited, ionized plasma produces the working gas atoms. In addition, the molecules are also produced. The nanosized droplets agglomerate into bigger grains during the Bi and Bi_2O_3 evaporation on the low-temperature forms, creating the continuous amorphous films. The amorphous phase's transformation into the crystalline phase reduces grain sizes for the deposited film at 200°C. The first nanoscale crystallite nucleation centres have begun to emerge.

The substrate temperatures provide the crystallization of the film using the energy supplied by the modification applied by annealing treatment. The oxygen concentration

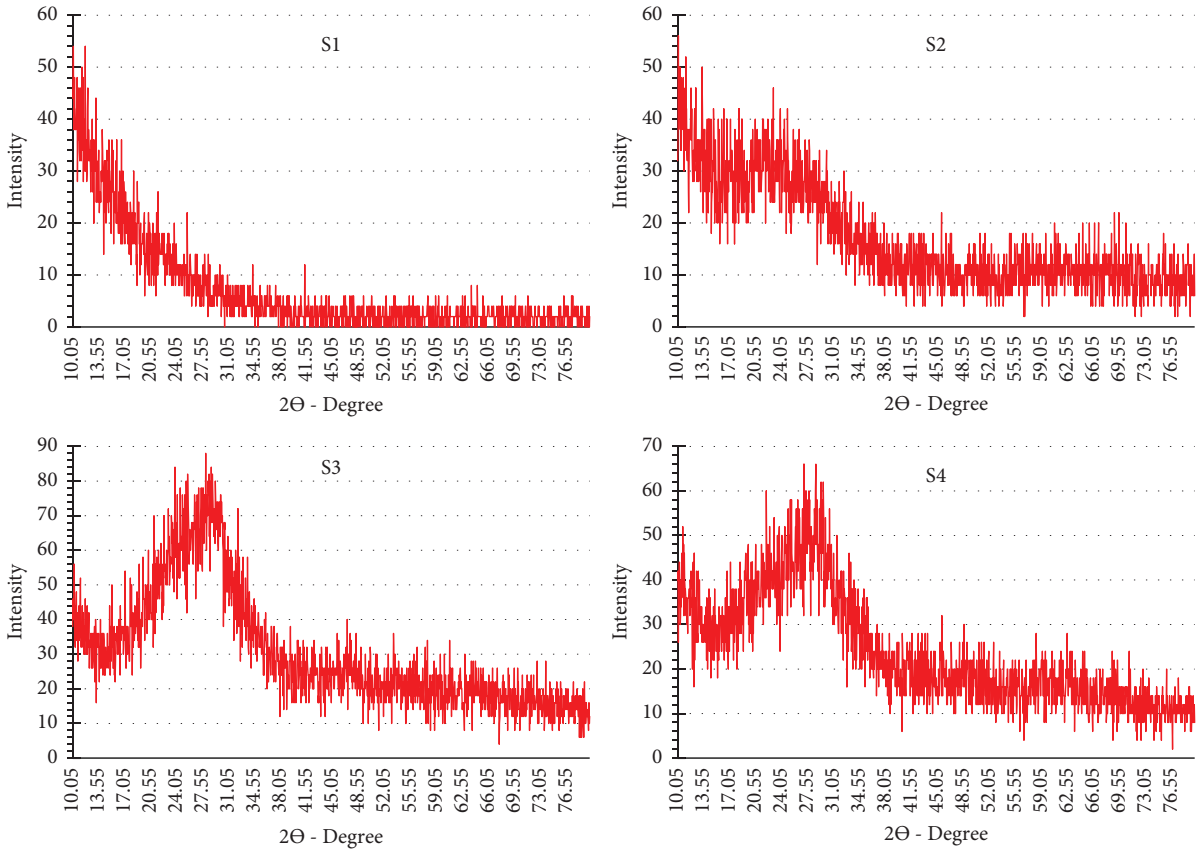

Figure 3: Bi_2O_3 sample XRD pattern (S1, S2, S3, and S4) preannealing treatment.

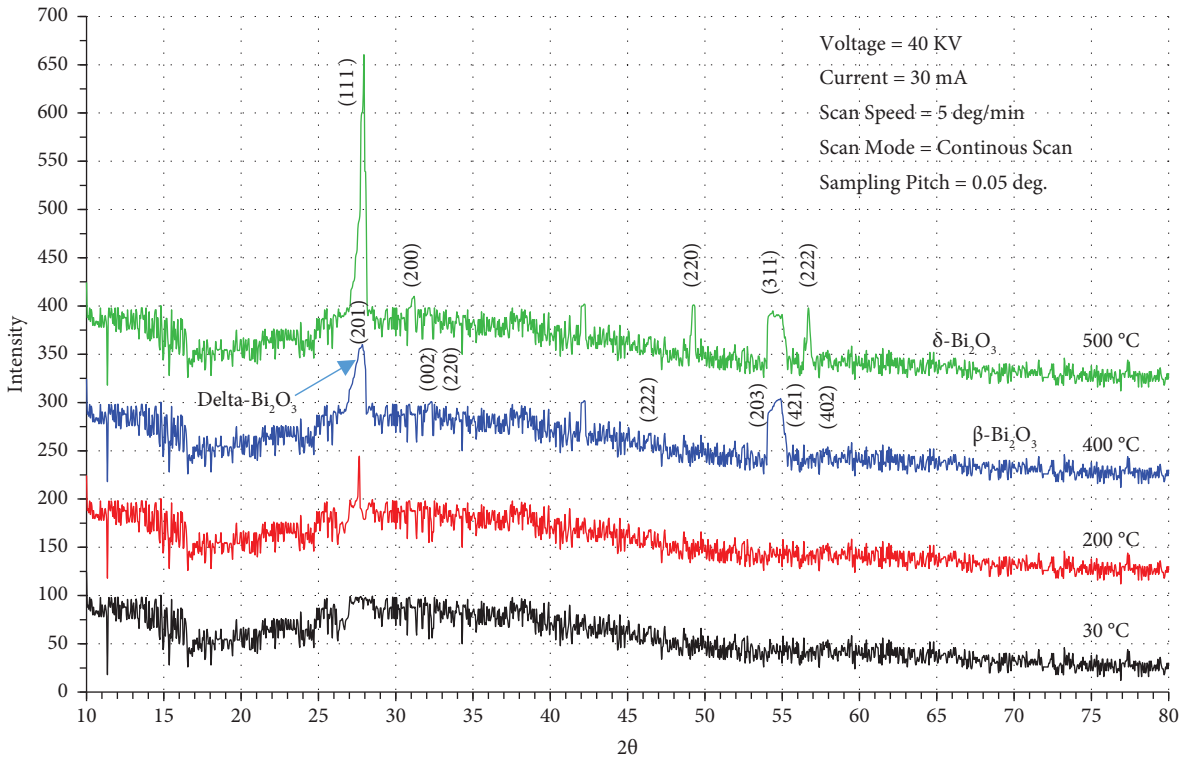

Figure 4: Bi_2O_3 film plasma XRD patterns sputtered on glass substrates assisted different annealing treatments.

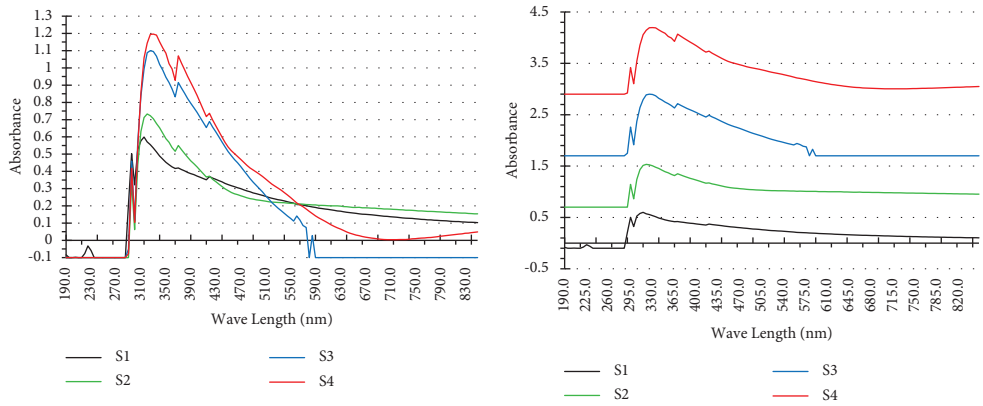

Figure 5: The UV-Vis spectrometer spectrum of the bismuth thin film preannealing process.

Table 1: The electrical resistivity of Bi_2O_3 films sputtered for 40 min with an annealing temperature for 2 hr.

Sample	Annealing temperature (°C)	Resistivity (10^{-3} Ωcm)
Bi preannealing	30	1.17
	150	1.10
	200	1.095
	250	0.67
	280	1.36
	300	2.58
	400	2.63
	500	2.71

increases in droplets with annealing in air, completely oxidizes, and functions as the centre nucleation of Bi_2O_3 nanostructures [56]. However, the under-study plasma sputtering system and conditions still need to be improved to develop crystalline Bi_2O_3 films in one step.

The bismuth thin film Ultraviolet-V's absorbance spectrum forms camel-like figures at 280 and 320 nm, with a little shift to the red region at 540 nm for the surface plasm on resonance and the light scatters (see Figure 5). The absorption coefficient with the annealing temperature is the postannealed thin film optical absorbance spectra at various annealing temperatures at the wavelength range of 300 to 1100 nm. There are many studies on high annealing temperature influence on Bi_xO_x films [57, 58]. According to the data, the annealing of the films at 300°C maximizes absorbance when there is extra annealing to 400°C, absorbance decreases in the annealed films at 500°C because of the rise of the film's roughness, and the following formula has been used to evaluate the bandgap [44, 59–64]:

$$(\alpha h\nu)2 = B(h\nu - Eg)n. \quad (1)$$

Here, α is the absorbance coefficient, $h\nu$ is the beam energy, B is the proportion constant, and Eg refers to energy gaps. Regarding Bi_2O_3 films, n equals 2 for direct allowed transition [65–67]. The Tauc method was used for the Bi_2O_3 optical band gaps to extrapolate the linear curve portions in the plot $(\alpha h\nu)2$ versus $h\nu$ [67]. The annealing temperature of the glass substrate changes the band gap of Bi_2O_3 formations. The film gap deposited at 30°C is 3 eV. As the Bi_2O_3thin-films glass slide annealing temperature rose to 200°C, the band gap shrunk to 2.70 eV. The band gap and temperature reached 3.05 eV and 500°C, respectively. The crystal structure, film thickness, and substrate temperature significantly impact the band gap values of Bi_2O_3 nanostructures and films confirmed by Salih et al. [68].

The exact mechanism by which the bandgap decreases during annealing can depend on the specific material and the annealing conditions, such as the annealing temperature and duration. However, it is essential to note that the relationship between band gap and grain size is only sometimes straightforward and can depend on several factors, including the specific material and the processing conditions used. Therefore, while a decrease in band gap and an increase in grain size coincide during annealing, it is not necessarily a universal rule that applies to all materials based on the current study data and, other studies [58, 59, 68]. In addition, upon film annealing at 500°C, the bandgap drops because of the nonstoichiometric Bi_2O_3 with a smaller bandgap [69, 70]. The rise in substrate temperature from 400°C to 500°C modifies the morphology of the surface, lowers the crystallite size, and transitions from β- Bi_2O_3 with a little amount of δ- Bi_2O_3 phase to pure δ- Bi_2O_3, which is the fundamental reason of Bi_2O_3 structures having excellent band gap values [67].

3.1. Electrical Characterization. The use of the D.C. two-probe method is to examine electrical resistivity as the sample temperature from (30–500)°C as Table 1 shows, and film preannealing at room temperature showed a resistivity of 1.2 × 10−3 Ωcm due to the charge carriers in Bi thin films scattered at the film surface and grain boundaries, keeping the same magnitude orders, and the lowest bismuth film resistance is (0.67 × 10−3 Ωcm) of 200–250°C, where the growth of bismuth films is possible even with no large particulates and segregating surfaces. The 250–280°C shows a considerable inconsistency in the calculated specimen. The properties of surface nucleation and adsorption transition at this range of temperatures and the bismuth film's electrical conductivity slightly enhanced only at 250°C. It is believed

that under our annealing conditions, changing the transport properties was not wholly possible (temperature and duration). Nevertheless, the electrical characteristics of the bismuth films exhibit an abrupt change when the temperature exceeds 280°C. The annealing was in the air atmosphere to prevent the oxidation and reaction of bismuth elements with oxygen adsorption on the film surface or in glass substrates; according to Leontie et al. [69], the thermal oxidation of bismuth forms amorphous oxide layers at the substrate-film interfaces on glass. Yet, the optical and electrical features were approximately between them, often determined by the structure nanometric sizes, in which intergrain flaws offer electrons to the optical transitions and the electrical conductivity.

4. Conclusion

Bi_2O_3 films are successfully deposited by bismuth target reactive sputtering at room temperature with fixed Ar/O_2 mixes. Also, the annealing treatment of bismuth films affects the deposited films' optical, structural, and electrical features. Then, the film deposition at less than 200°C makes Bi oxidized in $Bi \pm 3$ in completely amorphous transparent Bi_2O_3 films with the lowest conductivity responses. At 300–400°C, the place is the transition site where Bi reacts competently with oxygen, gaining moderately organized Bi_2O_3, which XRD examination proved. According to our experimental results, vacancies form at B (1) and O (2) sites in annealing where B (1) is possibly intrinsic while the second has a significant role in the RT stabilizing γ-Bi_2O_3. By the annealing approach with reactive plasma, assistance produces Bi_2O_3 films. Also, it creates nanostructures on glass substrates. The amorphous phases transitioned to the crystalline phase when the substrate temperature rose. Low-temperature growth of amorphous Bi_2O_3 films was followed by the formation of Bi_2O_3 nanostructures at 400 and 500°C. It was discovered that the temperatures of the substrate significantly affect the phase characteristics and Bi_2O_3 band gap. At 400°C, the mixed β-Bi_2O_3 and δ-Bi_2O_3 phase 3D Bi_2O_3 nanostructures were created. 3D nanostructures have a 3.05 eV band gap for 500°C annealing temperature. Nanowires formed and exhibited a 3.09 eV band gap made entirely of the δ-Bi_2O_3 phase, whose mean crystallite size is 38 nm. The electrical resistivity was boosted by 53% with elevated annealing temperatures up to 500°C. However, the absorbance also increased by annealing, which refers to an increase in the band gap and the crystal size at the maximum at 400°C.

Data Availability

The authors do not have the authority to share the data.

Conflicts of Interest

The authors declare that they have no conflicts of interest.

Acknowledgments

This study was self-funded by the authors

References

[1] T. Takeyama, N. Takahashi, T. Nakamura, and S. Itoh, "Microstructure characterization of δ-Bi2O3 thin film under atmospheric pressure by means of halide CVD on c-sapphire," *Journal of Crystal Growth*, vol. 275, no. 3-4, pp. 460–466, 2005.

[2] C. Karunakaran and R. Dhanalakshmi, "Semiconductor-catalyzed degradation of phenols with sunlight," *Solar Energy Materials and Solar Cells*, vol. 92, no. 11, pp. 1315–1321, 2008.

[3] R. R. S. Coronado-Castañeda, M. L. Maya-Treviño, E. Garza-González, J. Peral, M. Villanueva-Rodríguez, and A. Hernández-Ramírez, "Photocatalytic degradation and toxicity reduction of isoniazid using β-Bi2O3 in real wastewater," *Catalysis Today*, vol. 341, pp. 82–89, 2020.

[4] J. Xu, Y. Ao, D. Fu, and C. Yuan, "Synthesis of Bi2O3–TiO2 composite film with high-photocatalytic activity under sunlight irradiation," *Applied Surface Science*, vol. 255, no. 5, pp. 2365–2369, 2008.

[5] X. Gou, R. Li, G. Wang, Z. Chen, and D. Wexler, "Room-temperature solution synthesis of Bi2O3 nanowires for gas sensing application," *Nanotechnology*, vol. 20, no. 49, Article ID 495501, 2009.

[6] G. Hwang, "An electrochemical preparation of bismuth nanoparticles by reduction of bismuth oxide nanoparticles and their application as an environmental sensor," *Journal of Ceramic Processing Research*, vol. 10, no. 2, pp. 190–194, 2009.

[7] C. Wang, Y. Ao, P. Wang, J. Hou, and J. Qian, "Preparation, characterization and photocatalytic activity of the neodymium-doped TiO2 hollow spheres," *Applied Surface Science*, vol. 257, no. 1, pp. 227–231, 2010.

[8] S. S. Bhande, R. S. Mane, A. V. Ghule, and S.-H. Han, "A bismuth oxide nanoplate-based carbon dioxide gas sensor," *Scripta Materialia*, vol. 65, no. 12, pp. 1081–1084, 2011.

[9] Y. Komai, K. Okitsu, R. Nishimura et al., "Visible light response of nitrogen and sulfur co-doped TiO2 photocatalysts fabricated by anodic oxidation," *Catalysis Today*, vol. 164, no. 1, pp. 399–403, 2011.

[10] Z. Hamid, "Synthesis of Bismuth oxide Nano powders viaelectrolysis method and study the effect of change voltage on the size for it," *Aust. J. Basic Appl. Sci*, vol. 11, no. 7, pp. 97–101, 2017.

[11] S. Condurache-Bota, *Bismuth Oxide Thin Films for Optoelectronic and Humidity Sensing Applications*, Y. Zhou, F. Dong, and S. Jin, Eds., IntechOpen, London, UK, 2018.

[12] Z. Zhang, D. Gekhtman, M. S. Dresselhaus, and J. Y. Ying, "Processing and characterization of single-crystalline ultrafine bismuth nanowires," *Chemistry of Materials*, vol. 11, no. 7, pp. 1659–1665, 1999.

[13] M. Gutiérrez and A. Henglein, "Nanometer-sized Bi particles in aqueous solution: absorption spectrum and some chemical properties," *Journal of Physical Chemistry*, vol. 100, no. 18, pp. 7656–7661, 1996.

[14] S. Schulz, S. Heimann, C. Wölper, and W. Assenmacher, "Synthesis of bismuth pseudocubes by thermal decomposition of Bi2Et4," *Chemistry of Materials*, vol. 24, no. 11, pp. 2032–2039, 2012.

[15] E. E. Foos, R. M. Stroud, A. D. Berry, A. W. Snow, and J. P. Armistead, "Synthesis of nanocrystalline bismuth in reverse micelles," *Journal of the American Chemical Society*, vol. 122, no. 29, pp. 7114-7115, 2000.

[16] S. C. Warren, A. C. Jackson, Z. D. Cater-Cyker, F. J. DiSalvo, and U. Wiesner, "Nanoparticle synthesis via the

photochemical polythiol process," *Journal of the American Chemical Society*, vol. 129, no. 33, pp. 10072-10073, 2007.

[17] J. Shen, Y. Zhu, C. Chen, X. Yang, and C. Li, "Facile preparation and upconversion luminescence of graphene quantum dots," *Chemical Communications*, vol. 47, no. 9, pp. 2580–2582, 2011.

[18] R. Fu, S. Xu, Y.-N. Lu, and J.-J. Zhu, "Synthesis and characterization of triangular bismuth nanoplates," *Crystal Growth and Design*, vol. 5, no. 4, pp. 1379–1385, 2005.

[19] Y. Li, J. Wang, Z. Deng et al., "Bismuth nanotubes: a rational low-temperature synthetic route," *Journal of the American Chemical Society*, vol. 123, no. 40, pp. 9904-9905, 2001.

[20] R. Boldt, M. Kaiser, D. Köhler, F. Krumeich, and M. Ruck, "High-yield synthesis and structure of double-walled bismuth-nanotubes," *Nano Letters*, vol. 10, no. 1, pp. 208–210, 2010.

[21] C. J. Tang, G. H. Li, X. C. Dou, Y. X. Zhang, and L. Li, "Thermal expansion behaviors of bismuth nanowires," *Journal of Physical Chemistry C*, vol. 113, no. 14, pp. 5422–5427, 2009.

[22] Y. Wang and Y. Xia, "Bottom-up and top-down approaches to the synthesis of monodispersed spherical colloids of low melting-point metals," *Nano Letters*, vol. 4, no. 10, pp. 2047–2050, 2004.

[23] A. A. Najim, M. A. H. Muhi, K. R. Gbashi, and A. T. Salih, "Synthesis of efficient and effective γ-MnO2/α-Bi2O3/a-Si solar cell by vacuum thermal evaporation technique," *Plasmonics*, vol. 13, no. 3, pp. 891–895, 2018.

[24] X. Yang, X. Lian, S. Liu et al., "Visible light photoelectrochemical properties of β-Bi2O3 nanoporous films: a study of the dependence on thermal treatment and film thickness," *Applied Surface Science*, vol. 282, pp. 538–543, 2013.

[25] T. P. Gujar, V. R. Shinde, and C. D. Lokhande, "The influence of oxidation temperature on structural, optical and electrical properties of thermally oxidized bismuth oxide films," *Applied Surface Science*, vol. 254, no. 13, pp. 4186–4190, 2008.

[26] Y. Wang, Z. Li, H. Yu, and L. Guo, "Controllable synthesis of metastable γ-Bi2O3 architectures and optical properties," *Materials Science in Semiconductor Processing*, vol. 64, pp. 55–62, 2017.

[27] S. Bandyopadhyay, S. Dutta, A. Dutta, and S. K. Pradhan, "Mechanosynthesis of nanocrystalline fully stabilized bcc γ-phase of Bi2O3 without any additive: manifestation of ferroelasticity in microstructure, optical, and transport properties," *Crystal Growth and Design*, vol. 18, no. 11, pp. 6564–6572, 2018.

[28] Y. G. Bak, J. W. Park, Y. J. Park et al., "In-Zn-Sn-O thin film based transistor with high-k HfO2 dielectric," *Thin Solid Films*, vol. 753, Article ID 139290, 2022.

[29] M. Z. Ansari, P. Janicek, D. K. Nandi et al., "Low-temperature growth of crystalline Tin(II) monosulfide thin films by atomic layer deposition using a liquid divalent tin precursor," *Applied Surface Science*, vol. 565, Article ID 150152, 2021.

[30] M. Z. Ansari, P. Janicek, D. K. Nandi et al., "Influence of post-annealing on structural, optical and electrical properties of tin nitride thin films prepared by atomic layer deposition," *Applied Surface Science*, vol. 538, Article ID 147920, 2021.

[31] A. A. Najim, "Synthesis and characterization of bismite nano-island thin films for optoelectronic applications," *Materials Science in Semiconductor Processing*, vol. 121, Article ID 105334, 2021.

[32] H. S. Rasheed, H. I. Abdulgafour, F. M. Hassan, and A. A. Najim, "Synthesis, characterization, and gas-sensing performance of macroporous Zn-doped NiO thin films for ammonia gas detection," *Journal of Materials Science: Materials in Electronics*, vol. 33, no. 23, pp. 18187–18198, 2022.

[33] A. A. Najim, F. M. Hassan, H. S. Rasheed, H. Ismail, and H. H. Darwoysh, "Experimental investigation to determine the optical properties of (Fe2O3)1-x(NiO)x thin films prepared by PLD technique for NLO applications," *Optical Materials*, vol. 121, Article ID 111602, 2021.

[34] F. M. Hassan and A. U. S. A. Najim, "Synthesis and characterization of nanocrystalline co-doped zno thin films prepared by chemical spray pyrolysis for optoelectronic applications," *Surface Review and Letters*, vol. 28, no. 12, 2021.

[35] A. M. Mejbel, M. M. Khalaf, and A. M. Kwad, "Improving the machined surface of AISI H11 tool steel in milling process," *J. Mech. Eng. Res. Dev*, vol. 44, no. 4, pp. 58–68, 2021.

[36] M. K. Mejbel, H. R. Atwan, and I. T. Abdullah, "Void formation in friction stir welding of AA5052 butt joining," *Journal of Mechanical Engineering Research and Developments*, vol. 44, no. 5, pp. 318–332, 2021.

[37] T. H. Abood Al-Saadi, S. Hameed Mohammad, E. G. Daway, and M. K. Mejbel, "Synthesis of intumescent materials by alkali activation of glass waste using intercalated graphite additions," *Materials Today: Proceedings*, vol. 42, no. 5, pp. 1889–1900, 2021.

[38] M. Allawi, M. Mejbel, and M. Oudah, "Variable valve timing (VVT) modelling by Lotus engine simulation software," *International Journal of Automotive and Mechanical Engineering*, vol. 17, no. 4, pp. 8397–8410, 2021.

[39] A. A. Muhmmed, M. K. Hussain, A. R. Khudadad, H. H. Mahdi, and M. K. Mejbel, "Mechanical behavior of laser engraved single lap joints adhered by polymeric material," *International Review of Mechanical Engineering (IREME)*, vol. 15, no. 12, pp. 622–628, 2021.

[40] M. K. Mejbel, I. T. Abdullah, and K. T. Nabil, "Thin wall manufacturing improvement using novel simultaneous double-sided cutter milling technique," *International Journal of Automotive and Mechanical Engineering*, vol. 19, no. 1, pp. 6519–6529, 2022.

[41] A. A. Beddai, B. A. Badday, A. M. Al-Yaqoobi, M. K. Mejbel, Z. S. Al Hachim, and M. K. A. Mohammed, "Color removal of textile wastewater using electrochemical batch recirculation tubular upflow cell," *International Journal of Chemical Engineering*, vol. 2022, Article ID 4713399, 8 pages, 2022.

[42] S. A. J. Beden, A. A. Ati, K. A. F. Alimarah, S. K. Saihood, R. K. Abdulnabi, and M. K. Mejbel, "Green synthesis and characterization of silver nanoparticles/CM-chitosan-isopropanol by gamma irradiations method," *Revue des Composites et des Matériaux Avancés*, vol. 32, no. 4, pp. 173–180, 2022.

[43] M. K. Mejbel, M. K. Allawi, and M. H. Oudah, "Effects of WC, SiC, iron and glass fillers and their high percentage content on adhesive bond strength of an aluminium alloy butt joint: an experimental study," *Journal of Mechanical Engineering Research and Developments*, vol. 42, no. 5, pp. 224–231, 2019.

[44] S. A. J. Beden, H. I. Dambos, R. K. Abdulnabi, M. K. Mejbel, and N. K. Taieh, "NanoSilver/CS solutions optical characterizations and some applications," *Revue des Composites et des Matériaux Avancés*, vol. 33, no. 1, pp. 31–38, 2023.

[45] A. U. Moosa, E. Hernández-Nava, M. K. Mejbel, and I. Todd, "The joining of CP-vanadium and Ti–6Al–4V using the electron beam melting additive manufacturing method," *Advances in Industrial and Manufacturing Engineering*, vol. 5, Article ID 100102, 2022.

[46] T. H. Abood Al-Saadi, E. G. Daway, S. H. Mohammad, and M. K. Mejbel, "Effect of graphite additions on the intumescent behaviour of alkali-activated materials based on glass waste," *Journal of Materials Research and Technology*, vol. 9, no. 6, pp. 14338–14349, 2020.

[47] A. K. Ghazi, A. A. Muhmmed, N. K. Taieh, and M. K. Mejbel, "Tribological and mechanical performance of epoxy reinforced by fish scales powder," *Revue des Composites et des Matériaux Avancés*, vol. 32, no. 3, pp. 149–155, 2022.

[48] A. R. Baqer, A. A. Beddai, M. M. Farhan, B. A. Badday, and M. K. Mejbel, "Efficient coating of titanium composite electrodes with various metal oxides for electrochemical removal of ammonia," *Results in Engineering*, vol. 9, Article ID 100199, 2021.

[49] A. A. Al-Joubori, A. U. Moosa, and M. K. Mejbel, "Mechanically alloyed: synthesis of nanostructured intermetallic compound of zinc selenide," *Revue des Composites et des Matériaux Avancés*, vol. 33, no. 1, pp. 47–51, 2023.

[50] Al, R. K. Abdulnabi, M. N. Ismael, H. F. Hassan, and M. K. Mejbel, "Glass waste based geopolymers and their characteristics," *Revue des Composites et des Matériaux Avancés*, vol. 32, no. 1, pp. 17–23, 2022.

[51] T. H. A. Al Saadi, R. K. Abdulnabi, M. M. Khalaf, and M. K. Mejbel, "Synthesis of foaming materials from glass based geopolymers and yeast additives," *International Journal on Technical and Physical Problems of Engineering*, vol. 14, no. 4, pp. 289–297, 2022.

[52] B. Yang, M. Mo, H. Hu et al., "A rational self-sacrificing template route to β-Bi2O3 nanotube arrays," *European Journal of Inorganic Chemistry*, vol. 2004, pp. 1785–1787, 2004.

[53] X. Xiao, R. Hu, C. Liu et al., "Facile large-scale synthesis of β-Bi2O3 nanospheres as a highly efficient photocatalyst for the degradation of acetaminophen under visible light irradiation," *Applied Catalysis B: Environmental*, vol. 140-141, no. 141, pp. 433–443, 2013.

[54] M. I. Mohammed, M. K. Ismael, and M. Gönen, "Synthesis of chitosan-silica nanocomposite for removal of methyl orange from water: composite characterization and adsorption performance," *IOP Conference Series: Materials Science and Engineering*, vol. 745, no. 1, Article ID 012084, 2020.

[55] M. I. Mohammad, A. A. Moosa, J. H. Potgieter, and M. K. Ismael, "Carbon nanotubes synthesis via arc discharge with a yttria catalyst," *ISRN Nanomaterials*, vol. 2013, Article ID 785160, 7 pages, 2013.

[56] B. Ling, X. W. Sun, J. L. Zhao et al., "One-dimensional single-crystalline bismuth oxide micro/nanoribbons: morphology-controlled synthesis and luminescent properties," *Journal of Nanoscience and Nanotechnology*, vol. 10, no. 12, pp. 8322–8327, 2010.

[57] L. Scholtz, L. Ladanyi, and J. Mullerova, "Influence of surface roughness on optical characteristics of multilayer solar cells," *Advances in Electrical and Electronic Engineering*, vol. 12, no. 6, 2015.

[58] A. A. Najim, H. H. Darwoysh, Y. Z. Dawood, S. Q. Hazaa, and A. T. Salih, "Structural, topography, and optical properties of Ba-doped Mn3O4 thin films for ammonia gas sensing application," *Physica Status Solidi (A)*, vol. 215, no. 24, Article ID 1800379, 2018.

[59] C. V. Ramana, R. J. Smith, and O. M. Hussain, "Grain size effects on the optical characteristics of pulsed-laser deposited vanadium oxide thin films," *Physica Status Solidi (A)*, vol. 199, no. 1, pp. R4–R6, 2003.

[60] H. Mikhlif, M. Dawood, O. Abdulmunem, and M. K. Mejbel, "Preparation of high-performance room temperature ZnO nanostructures gas sensor," *Acta Physica Polonica, A*, vol. 140, no. 4, pp. 320–326, 2021.

[61] S. J. Mezher, M. O. Dawood, O. M. Abdulmunem, and M. K. Mejbel, "Copper doped nickel oxide gas sensor," *Vacuum*, vol. 172, Article ID 109074, 2020.

[62] S. J. Mezher, M. O. Dawood, A. A. Beddai, and M. K. Mejbel, "NiO nanostructure by RF sputtering for gas sensing applications," *Materials Technology*, vol. 35, no. 1, pp. 60–68, 2020.

[63] W. J. Aziz, M. A. Abid, D. A. Kadhim, and M. K. Mejbel, "Synthesis of iron oxide (β-fe2o3) nanoparticles from Iraqi grapes extract and its biomedical application," *IOP Conference Series: Materials Science and Engineering*, vol. 881, no. 1, Article ID 012099, 2020.

[64] S. J. Mezher, K. J. Kadhim, O. M. Abdulmunem, and M. K. Mejbel, "Microwave properties of Mg–Zn ferrite deposited by the thermal evaporation technique," *Vacuum*, vol. 173, Article ID 109114, 2020.

[65] M. G. Hale, R. Little, M. A. Salem, J. H. Hedley, B. R. Horrocks, and L. Šiller, "Formation of bismuth oxide nanowires by simultaneous templating and electrochemical adhesion of DNA on Si/SiO2," *Thin Solid Films*, vol. 520, no. 24, pp. 7044–7048, 2012.

[66] N. M. Ravindra, P. Ganapathy, and J. Choi, "Energy gap–refractive index relations in semiconductors – an overview," *Infrared Physics and Technology*, vol. 50, no. 1, pp. 21–29, 2007.

[67] A. Iljinas, S. Burinskas, and J. Dudonis, "Synthesis of bismuth oxide thin films deposited by reactive magnetron sputtering," *Acta Physica Polonica*, vol. 120, no. 1, pp. 60–62, 2011.

[68] A. T. Salih, A. A. Najim, M. A. H. Muhi, and K. R. Gbashi, "Single-material multilayer ZnS as anti-reflective coating for solar cell applications," *Optics Communications*, vol. 388, pp. 84–89, 2017.

[69] L. Leontie, M. Caraman, M. Alexe, and C. Harnagea, "Structural and optical characteristics of bismuth oxide thin films," *Surface Science*, vol. 507–510, no. 510, pp. 480–485, 2002.

[70] S. Condurache-Bota, N. Tigau, M. Praisler, G. Prodan, and R. Gavrila, "Near-infrared energy bandgap bismuth oxide thin films and their in-depth morpho-structural and optical analysis," *Romanian Reports in Physics*, vol. 69, no. 3, pp. 1–10, 2017.